

Electron energy distributions in a magnetized inductively coupled plasma

Sang-Heon Song,^{1,a)} Yang Yang,^{2,b)} Pascal Chabert,^{3,c)} and Mark J. Kushner^{4,d)}

¹Department of Nuclear Engineering and Radiological Sciences, University of Michigan, 2355 Bonisteel Boulevard, Ann Arbor, Michigan 48109-2104, USA

²Applied Materials Inc., 974 E. Arques Avenue, M/S 81312, Sunnyvale, California 94085, USA

³LPP, CNRS, Ecole Polytechnique, UPMC, Paris XI, 91128 Palaiseau, France

⁴Department of Electrical Engineering and Computer Science, University of Michigan, 1301 Beal Avenue, Ann Arbor, Michigan 48109-2122, USA

(Received 22 July 2014; accepted 11 September 2014; published online 26 September 2014)

Optimizing and controlling electron energy distributions (EEDs) is a continuing goal in plasma materials processing as EEDs determine the rate coefficients for electron impact processes. There are many strategies to customize EEDs in low pressure inductively coupled plasmas (ICPs), for example, pulsing and choice of frequency, to produce the desired plasma properties. Recent experiments have shown that EEDs in low pressure ICPs can be manipulated through the use of static magnetic fields of sufficient magnitudes to magnetize the electrons and confine them to the electromagnetic skin depth. The EED is then a function of the local magnetic field as opposed to having non-local properties in the absence of the magnetic field. In this paper, EEDs in a magnetized inductively coupled plasma (mICP) sustained in Ar are discussed with results from a two-dimensional plasma hydrodynamics model. Results are compared with experimental measurements. We found that the character of the EED transitions from non-local to local with application of the static magnetic field. The reduction in cross-field mobility increases local electron heating in the skin depth and decreases the transport of these hot electrons to larger radii. The tail of the EED is therefore enhanced in the skin depth and depressed at large radii. Plasmas densities are non-monotonic with increasing pressure with the external magnetic field due to transitions between local and non-local kinetics. © 2014 AIP Publishing LLC.

[<http://dx.doi.org/10.1063/1.4896711>]

I. INTRODUCTION

Magnetic fields have been used in a variety of low pressure plasma applications in order to manipulate not only the spatial distribution but also the peak values of electron temperature and density. In the context of plasma materials processing, plasma sources using magnetic fields include electron cyclotron resonance (ECR) discharges,^{1,2} magnetically enhanced reactive ion etching (MERIE) systems,³ helicon discharges,⁴ and magnetrons.⁵ Computational investigations of these systems have been conducted to provide an improved understanding of the flow of power through these partially ionized magnetized plasmas.^{6,7} Although these plasmas have been developed for different materials processing applications—etching, deposition, implantation—the fundamental motivation behind using magnetic fields is controlling the spatial and energy distributions of electrons, ions, and neutrals.^{8–21}

Electron kinetics are often described as being *local* or *nonlocal*. Local electron kinetics is typically observed in high pressure systems where the electron energy relaxation

length λ_e is smaller than the characteristic skin depth of the electromagnetic field, δ , or chamber size L .²² In non-local kinetics, λ_e is sufficiently large that the electron energy distribution (EED) based on total energy (kinetic energy plus potential energy) is essentially uniform across the chamber. In some sense, the electron acceleration and energy loss processes appear to be localized in different volumes of the plasma. The spatial distribution of the electric field that produces electron heating is not strongly correlated with the spatial distribution of plasma parameters, such as temperature and EED. Controlling whether electron transport is local or non-local provides an opportunity to control the spatial distribution of EEDs.²³ For example, if electron transport is local, then EEDs will have extended tails dominantly where power is deposited, as in the skin depth of an inductively coupled plasma (ICP). If electron transport is non-local, the tail may be extended far away from the skin depth. Application of an external, static magnetic field modifies plasma transport and its electrostatics, and can considerably reduce λ_e across magnetic field lines. In doing so, electron kinetics can appear to transition from being non-local to being local.^{15,16}

Rehman *et al.*²⁰ calculated power absorption in a magnetized inductively coupled plasma using a fluid method. They demonstrated the propagation of electromagnetic waves along the direction of the external magnetic field. They also observed negative power deposition, which originates from opposing phases of current and electric field due

^{a)}Present address: TEL Technology Center America, NanoFab South 300, 255 Fuller Road, Suite 244, Albany, New York 12203, USA. Electronic addresses: ssongs@umich.edu and Sang-Heon.Song@us.tel.com

^{b)}yang_yang@amat.com

^{c)}pascal.chabert@lpp.polytechnique.fr

^{d)}Author to whom correspondence should be addressed. Electronic mail: mjkush@umich.edu

to the thermal motion of the electrons.²⁴ Particle-in-cell/Monte-Carlo collision (PIC/MCC) methods have been used to investigate magnetized plasmas for materials processing, and, in particular, to predict EEDs. Kim *et al.*²¹ computationally obtained EEDs in a dual-frequency capacitively coupled plasma with a magnetic field. They showed the heating of low-energy electrons due to confinement by the magnetic field.

In low pressure inductively coupled plasmas, electron energy transport is largely non-local. In spite of this non-local transport, power deposition and ionization frequency are larger in the skin depth of the evanescent rf field into the plasma.²⁵ The difference between plasma properties in the bulk and in the skin depth result from relatively small changes in the tail of the EEDs. Pulsing of ICPs^{26,27} and changing the frequency of the rf power^{23,28} can be used to customize EEDs. However, even with these techniques, it is still difficult to control the spatial distribution of the EEDs in the absence of increasing gas pressure, conditions that produce $\lambda_e \ll L$. Use of static magnetic fields is a means of controlling λ_e and so controlling the character of electron transport between non-local and local. For example, EED control was demonstrated in a 10 mTorr ICP sustained in argon having a transverse magnetic field of 245 G.¹⁵ The electron temperature monotonically decreased along the positive gradient of the magnetic field. This technique, known as magnetic filtering, is also used in negative ion sources to locally reduce the electron temperature near the aperture through which ions are extracted.²⁹

Global magnetic filtering and control of EEDs in low pressure ICPs was demonstrated by Godyak²³ and Monreal *et al.*¹⁶ In these experiments, the inductive plasma was generated by a re-entrant antenna excited at 5 MHz. A coaxial cylindrical permanent magnet produced a static dipole magnetic field having a decay length commensurate with the electromagnetic skin depth. They found that the magnetic field created non-local electron transport conditions which enabled manipulation of the local EEDs. For a constant power deposition with a magnetic field, there were increased populations of hot electrons that were magnetically confined in the vicinity of the antenna (larger magnetic fields) and populations of cold electrons able to escape the magnetic barrier remote from the coil (smaller magnetic fields).

In this paper, we discuss results from a computational investigation of EEDs in magnetically enhanced inductively coupled plasmas (mICPs) for the experimental conditions of Monreal *et al.*¹⁶ and Godyak.²³ The model used in this investigation is a kinetic-fluid hybrid simulation. EEDs are produced with the kinetic portion of the model whereas plasma densities are produced in the fluid portion of the model. To address the magnetized plasmas in this study, we developed a fully implicit solution for the electron continuity equation combined with a semi-implicit solution for Poisson's equation. To speed the calculation, the electron transport algorithms in the electron kinetics portions of the model were also made computationally parallel. Other portions of the model that were computationally taxing, such as successive-over-relaxation routines for matrix algebra, were also made parallel.

The computed trends for EEDs with and without the magnetic field for ICPs sustained in 3 mTorr of Ar show a quantitative agreement with the experiment and so confirm the ability to control EEDs. The model used in this study is described in Sec. II. The typical plasma properties in magnetized ICPs are discussed in Sec. III, and scaling with pressure and power are shown in Sec. IV. Our concluding remarks are in Sec. V.

II. DESCRIPTION OF THE MODEL

The model used in this investigation is a two-dimensional kinetic-fluid hydrodynamics simulation that combines separate modules that address different physical phenomena in an iterative manner.³⁰ The modules used in this study include the electromagnetic module (EMM), the fluid kinetics-Poisson module (FKPM), the electron energy transport module (EETM) utilizing an electron Monte Carlo simulation (eMCS), and the Monte Carlo radiation transport module (MCRTM). The EMM calculates inductively coupled electric and magnetic fields (from antenna coils) as well as static magnetic fields produced by dc magnetic coils or permanent magnets. In the FKPM, separate continuity, momentum, and energy equations are simultaneously integrated in time for all heavy particle species (neutral and charged).

All electron transport coefficients and rate coefficients for electron impact collisions are provided by the EETM using the eMCS, which also provides EEDs as a function of position. In the eMCS, we integrate the trajectories of pseudoparticles given the spatially and time varying electric and magnetic fields (both static and electromagnetic) while statistically including velocity and energy changing collisions. So this method is a direct, statistical solution to the collisional Boltzmann's equation for EEDs. The eMCS including electron-neutral, electron-ion, and electron-electron collisions is described in Ref. 31. The method used here is essentially the same as in Ref. 31 with the exception that the Lorentz equation is used to advance the trajectories of the pseudoparticles. For particle i at location \vec{r} ,

$$m_i \frac{d\vec{v}_i(\vec{r}, t)}{dt} = q(\vec{E}_S(\vec{r}, t) + \vec{E}_\omega(\vec{r}, t)) + q\vec{v}_i(\vec{r}, t) \times (\vec{B}_S(\vec{r}) + \vec{B}_\omega(\vec{r}, t)), \quad (1)$$

where m_i is the particle's mass, $\vec{E}_S(\vec{r}, t)$ is the two-dimensional (r, z) electrostatic field produced in the FKPM and $\vec{B}_S(\vec{r})$ is the 2d externally applied magnetostatic field. $\vec{E}_\omega(\vec{r}, t)$ and $\vec{B}_\omega(\vec{r}, t)$ are the 3d (r, z, θ) harmonic electromagnetic fields produced by the EMM. The antenna currents are applied to the ICP reactor are in the azimuthal (θ) direction while the $\vec{B}_S(\vec{r})$ is applied in the (r, z) directions—the combination of which produces 3-components (r, z, θ) of both $\vec{E}_\omega(\vec{r}, t)$ and $\vec{B}_\omega(\vec{r}, t)$. Although the model is in 2d (r, z) for densities, electron energy transport in the eMCS is performed in 3d to capture electron cyclotron motion and the consequences of the 3-components of $\vec{E}_\omega(\vec{r}, t)$ and $\vec{B}_\omega(\vec{r}, t)$.

In practice, $\vec{E}_\omega(\vec{r}, t)$ and $\vec{B}_\omega(\vec{r}, t)$ are transferred to the eMCS as spatially dependent amplitudes and phases. The phase of each pseudoparticle in the rf cycle during integration of its trajectory is then used to obtain the local electromagnetic fields. Although these fields are computed in cylindrical coordinates, they are converted to Cartesian form to advance the trajectories of the pseudoparticles, which are tracked in 3D Cartesian space.

The method of solving the wave equation with static magnetic fields is described in Ref. 32. Briefly, the form of the wave equation solved is

$$\nabla \cdot \frac{1}{\mu} \nabla \vec{E} + \omega^2 \varepsilon \vec{E} = i\omega \vec{j}, \quad (2)$$

where μ is the permeability, \vec{E} is the electric field, ω is the frequency of the source current, ε is the permittivity, and \vec{j} is the current density. Only the harmonic electron current is retained in the plasma due to the low mobility of ions. When using fluid techniques to model plasma transport using the drift-diffusion approximation in the presence of static magnetic fields, tensor forms of the transport coefficients (e.g., conductivity, mobility, and diffusion coefficient) are used. With the tensor forms of the transport coefficients, the electron current density is expressed as³³

$$\vec{j} = q(n_e \bar{\mu} \vec{E} - \bar{D} \nabla n_e), \quad (3)$$

where q is the electron charge, n_e is the electron density, and $\bar{\mu}$ and \bar{D} are the tensor forms of the mobility and diffusion coefficients. Although Eq. (3) is strictly applicable to local electron transport, the kinetic electron energy transport in the plasma modules does capture non-local kinetics. The tensor forms of the transport coefficients, \bar{A} , are derived from their isotropic values, A_0 , by

$$\bar{A} = \frac{A_0}{\alpha^2 + |B|^2} \times \begin{pmatrix} \alpha^2 + B_r^2 & \alpha B_z + B_r B_\theta & -\alpha B_\theta + B_r B_z \\ -\alpha B_z + B_r B_\theta & \alpha^2 + B_\theta^2 & \alpha B_r + B_\theta B_z \\ \alpha B_\theta + B_r B_z & -\alpha B_r + B_\theta B_z & \alpha^2 + B_z^2 \end{pmatrix}, \quad (4)$$

$$\alpha = \frac{m_e(\nu_e + i\omega)}{q},$$

where B is the static applied magnetic field, q is the unit electron charge, m_e is the electron mass, and ν_e is the effective momentum collision frequency. The electromagnetic fields, $E(r, z, \theta)$ and $B(r, z, \theta)$, in the entire volume of the reactor, are solved by using a conjugate gradient method using a sparse matrix technique.³⁴ By setting $\nabla \cdot \vec{E} = 0$ to derive Eq. (2), we have ignored the consequences of the electrostatic Trivelpiece-Gould (TG) mode on plasma heating, which is known to play a role in the electron heating at small magnetic field (<20 G). We included a term for Landau damping, as described by Chen.³⁵ The effective electron collision frequency is then the sum of the conventional momentum transfer collision frequency (ν_m) and the Landau damping frequency (ν_{LD}).

The equations solved for ion transport (continuity, momentum, and energy) in the FKPM are

$$\frac{\partial N_i}{\partial t} = -\nabla \cdot \vec{\phi}_i + S_i - \left[\sum_j \gamma_{ij} (\nabla \cdot \vec{\phi}_j) \right]_S, \quad (5)$$

$$\begin{aligned} \frac{\partial \vec{\phi}_i}{\partial t} &= \frac{\partial(N_i \vec{v}_i)}{\partial t} \\ &= -\frac{1}{m_i} \nabla(k N_i T_i) - \nabla \cdot (N_i \vec{v}_i \vec{v}_i) + \frac{q_i N_i}{m_i} \times (\vec{E} + \vec{v}_i \times \vec{B}) \\ &\quad - \sum_j \frac{m_j}{m_i + m_j} N_i N_j (\vec{v}_i - \vec{v}_j) \nu_{ij} + S_i, \end{aligned} \quad (6)$$

$$\begin{aligned} \frac{\partial(N_i \varepsilon_i)}{\partial t} &= -\nabla \cdot (-\bar{\kappa} \nabla T_i - P_i \nabla \cdot \vec{v}_i - \nabla \cdot (N_i \vec{v}_i \varepsilon_i) + q_i \vec{\phi}_i \cdot \vec{E}) \\ &\quad - \sum_{m,j} k_{mij} N_j N_i \varepsilon_i + \sum_{m,j,l} K_{mjl} N_j N_l \Delta \varepsilon_{mj} \\ &\quad - \sum_j k_{ij}^m (\varepsilon_i - \varepsilon_j) N_j N_i \end{aligned} \quad (7)$$

$$\frac{\partial \rho_S}{\partial t} = -\nabla \cdot \sigma \vec{E} + \sum_j q_j s_j (\nabla \cdot \vec{\phi}_j) - \sum_j q_e \gamma_{ej} (\nabla \cdot \vec{\phi}_j), \quad (8)$$

where $\vec{\phi}_i$ is the flux of species i having density N_i , velocity \vec{v}_i , mass m_i , temperature T_i , pressure P_i , and total energy ε_i . k_{mij} is the rate coefficient for the m^{th} process for collisions between species i and j that remove species i , K_{mjl} is the rate coefficient for the m^{th} process for collisions between species j and l that create species i with energy $\Delta \varepsilon_{mj}$ and k_{ij}^m is the rate coefficient for momentum transfer (including mass ratios) between species i and j which at sufficient pressures results in temperature equilibration. S_i is the source for species i due to gas phase collision processes, γ_{ij} is the probability of producing species i by collision of species j on a surface, ν_{ij} is the momentum transfer collision frequency between species i and j , and $\bar{\kappa}$ is the tensor thermal conductivity. ρ_S is the charge density residing on and inside materials, σ is the material conductivity, q_j is the charge of species j having neutralization probability s_j on surfaces, and γ_{ej} is the secondary electron emission coefficient for ions, excited states, and photons.

The electron continuity and Poisson's equation are solved implicitly and simultaneously in the same matrix. This method provides the closest coupling between the electric potential and the electron density. The electron continuity equation is expressed as

$$\begin{aligned} n_e^{t+\Delta t} &= n_e^t + \Delta t \frac{\partial n_e^{t+\Delta t}}{\partial t}, \\ \frac{\partial n_e^{t+\Delta t}}{\partial t} &= -\nabla \cdot \left(-\bar{D}_e \nabla n_e^{t+\Delta t} - n_e \bar{\mu}_e \nabla \Phi^{t+\Delta t} \right) + S_{etotal}, \end{aligned} \quad (9)$$

where $\Phi^{t+\Delta t}$ and $n_e^{t+\Delta t}$ are the potential and electron density evaluated at $t + \Delta t$, and \bar{D}_e and $\bar{\mu}_e$ are the diffusion constant and the mobility of electrons in tensor form. S_{etotal} is the total source of electrons including the contributions from secondary electrons, electron impact ionization, photoionization, and heavy particle reactions such as Penning reactions. S_{etotal} is held constant during the actual integration step and is updated prior to the next integration step. The implicitness is achieved by numerically deriving Jacobian elements. The form of Poisson's equation solved is

$$\begin{aligned}
& -\nabla \cdot (\epsilon \nabla \Phi^{t+\Delta t}) \\
& = \rho_s' + \sum_i q_i N_i' + \Delta t \cdot \left[\frac{\partial \rho_s'}{\partial t} - q_e \nabla \right. \\
& \quad \times \left(\vec{\phi}_e(t) + \frac{\partial \vec{\phi}_e}{\partial \Phi} [\Phi^{t+\Delta t} - \Phi] \right) \\
& \quad \left. - \sum_j q_j \left[\nabla \cdot \left(\vec{\phi}_j(t) + \frac{\Delta t}{2} \frac{\partial \vec{\phi}_j(t)}{\partial t} \right) + S_j \right] \right], \quad (10)
\end{aligned}$$

where ρ_s is the charge density on surfaces and in materials, ϵ is the local permittivity either in the plasma, non-plasma gases or materials, and $\vec{\phi}_e$ and $\vec{\phi}_j$ are the flux of electrons and ions. $\vec{\phi}_j$ for ions is provided by separate momentum equations. ρ_s and N_i are evaluated at t , while potentials are evaluated at $t + \Delta t$, thereby providing implicitness. The last sum in Eq. (10) includes a prediction for ion fluxes by the momentum equations at $t + \Delta t$. The time derivative of the ion flux $\frac{\partial \phi_{i,j}(t)}{\partial t}$ is numerically produced by retaining a time-history of ion fluxes provided or by the most recent value provided by Eq. (6). Jacobian elements $\frac{\partial \vec{\phi}_e}{\partial \Phi}$ in Eq. (10) are the first-order partial derivatives of the function $\vec{\phi}_e$ with respect to Φ . Here, Jacobian elements are numerically evaluated by perturbing Φ a small fractional value and computing the change in $\vec{\phi}_e$. For example, due to the finite differencing method used, each component of electron flux $\phi_{i,j}$ at a location (i, j) in the structured numerical mesh is a function of the electrostatic potentials at that mesh point and all adjacent mesh points, which produces a 9-point numerical molecule and 9 terms in the sum over Jacobian elements in Eq. (10). The Jacobian element for $\Phi_{i+1,j}$ is derived from

$$\frac{\partial \phi_{i,j}}{\partial \Phi_{i+1,j}} = \frac{\phi_{i,j}(\Phi_{i+1,j} + \Delta \Phi_{i+1,j}) - \phi_{i,j}(\Phi_{i+1,j})}{\Delta \Phi_{i+1,j}}, \quad (11)$$

where $\Delta \Phi_{i+1,j}$ is a predefined perturbation, which is typically 5% of the current value. The incomplete *LU* biconjugate gradient sparse matrix technique is used to simultaneously solve Eqs. (9) and (10).

The plasma source modeled in this investigation is a mICP sustained in argon. The species in the simulation are Ar, Ar(1s₂), Ar(1s₃), Ar(1s₄), Ar(1s₅), Ar(3p⁵ 4p), Ar(3p⁵ 4d), Ar⁺, Ar₂⁺, and the excimer dimer Ar₂^{*}. The reaction mechanism includes radiation transport, photoionization, electron ion impact excitation and ionization, electron ion recombination, heavy particle mixing of 1s_n levels, Penning ionization, associative and dissociative Penning ionization, symmetric charge exchange, and 3-body dimer formation. Photon transport is calculated in the MCRTM where the rates of photon absorption and re-emission are recorded for each optical transition, and are used to calculate radiation trapping factors that lengthen the natural lifetime of the emitting species. A detailed description of the MCRTM is in Ref. 36. Photoionization of all excited states due to VUV transitions at 106.66 nm (Ar(1s₄) → Ar) and 104.82 nm (Ar(1s₂) → Ar) is included.³⁷ The rate coefficients for heavy particle mixing and Penning ionization are obtained from Ref. 38. The Ar₂⁺ ions are mainly created by Hornbeck-Molnar and associative Penning ionization.³⁹

III. PLASMA PROPERTIES IN A MAGNETIZED ICP

The two-dimensional, cylindrically symmetric reactor used in this investigation is schematically shown in Fig. 1(a) and is patterned after the reactor described in Ref. 16. A permanent magnet is placed coaxially inside the antenna coil housed in a reentrant Pyrex cavity (30 mm inner diameter and 1 mm thick) immersed into the plasma. To increase coupling efficiency between the coil and the plasma, the thickness of the Pyrex was chosen to be thin. The radius and height of the chamber are 6 cm and 12 cm. The mid-height of the coil is at 6.3 cm. The coil was designed in the experiment to minimize capacitive coupling. In the model, we generate the plasma purely inductively at 5 MHz. We extended our computational domain beyond the outside of the plasma chamber (up to 12 cm) in order to properly represent the electrical and magnetic boundary conditions at the outer Pyrex wall of the plasma chamber (6 cm radius). For

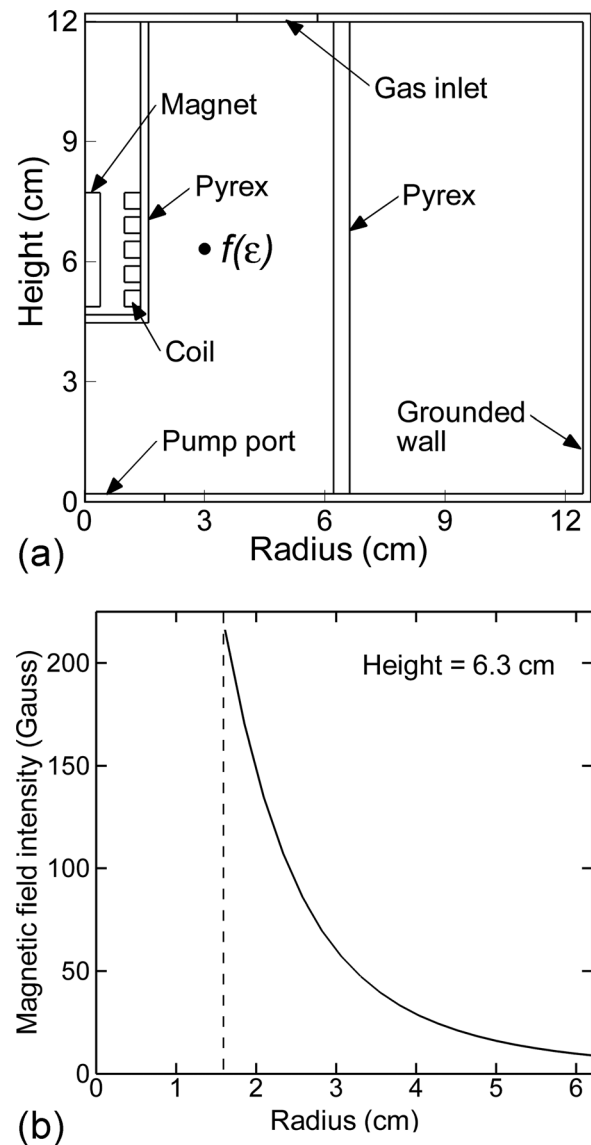


FIG. 1. Properties of the magnetically enhanced ICP. (a) Geometry of the mICP chamber. The permanent magnet is placed inside the antenna coil which is immersed in the plasma. (b) The magnetic field intensity at height of 6.3 cm as a function of radial position.

calculating the static magnetic field, the numerical mesh is extended axially by 50% above and below the normal computational domain, and in radius by 50%. The base case operating conditions are 3 mTorr of Ar with a flow rate of 1 sccm and power deposition of 100 W. Gas was injected annularly at the top and pumped on axis at the bottom. The strength of the magnet was chosen to produce a field of 100 Gauss at a radius of 2.4 cm, as shown in Fig. 1(b). At mid-height of the coil, the applied magnetic field is dominantly in the axial direction.

The amplitude of the azimuthal component of the inductively coupled electric fields and power deposition for the base case with and without the externally applied magnetic field, B_{ext} , are shown in Fig. 2. In the absence of the magnetic field, the maximum power deposition is $2.8 \text{ W}\cdot\text{cm}^{-3}$ and is restricted to a skin depth of 1.0 cm. The azimuthal

electric field in the plasma 1 mm from the inner dielectric surface is $E_\theta = 10 \text{ V/cm}$. With B_{ext} , the maximum power deposition decreases to $0.4 \text{ W}\cdot\text{cm}^{-3}$ while the volume over which significant power is more extended. In the absence of B_{ext} , E_θ is the only component of the inductive electric field. With B_{ext} , all three components of the inductive electric field are generated due to the tensor conductivity and the power deposition extends to a larger radius. With B_{ext} , conductivity in the azimuthal direction is significantly reduced due to the axial component of the magnetic field. E_θ therefore increases to maintain the desired power deposition.⁴⁰

The electron density, n_e , and electron temperature, T_e , for the base case with and without B_{ext} are shown in Fig. 3. The electron impact ionization source, S_e , is shown in Fig. 4. With B_{ext} , the peak electron density increases by a factor of more than 20 (from $2.5 \times 10^{10} \text{ cm}^{-3}$ to $5.3 \times 10^{11} \text{ cm}^{-3}$) and

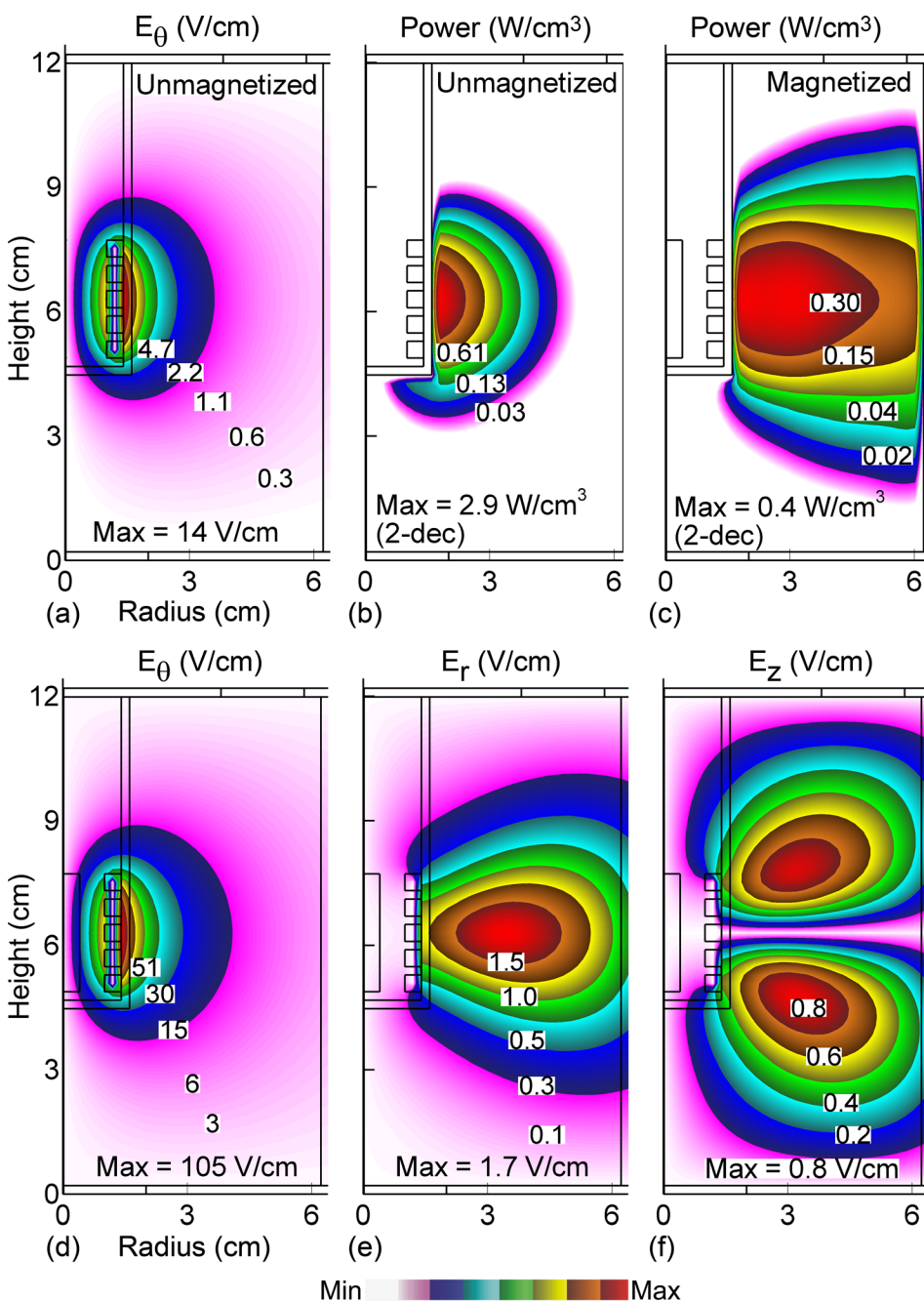


FIG. 2. Power deposition and electric fields for the base case conditions (3 mTorr, 100 W, 5 MHz). (a) Azimuthal electric field without B_{ext} , (b) power deposition without B_{ext} , (c) power deposition with B_{ext} ; and electric fields with B_{ext} (d) azimuthal, (e) radial, and (f) axial. The azimuthal electric field is larger with B_{ext} in order to compensate for the reduced conductivity. The power absorbing volume is larger with B_{ext} .

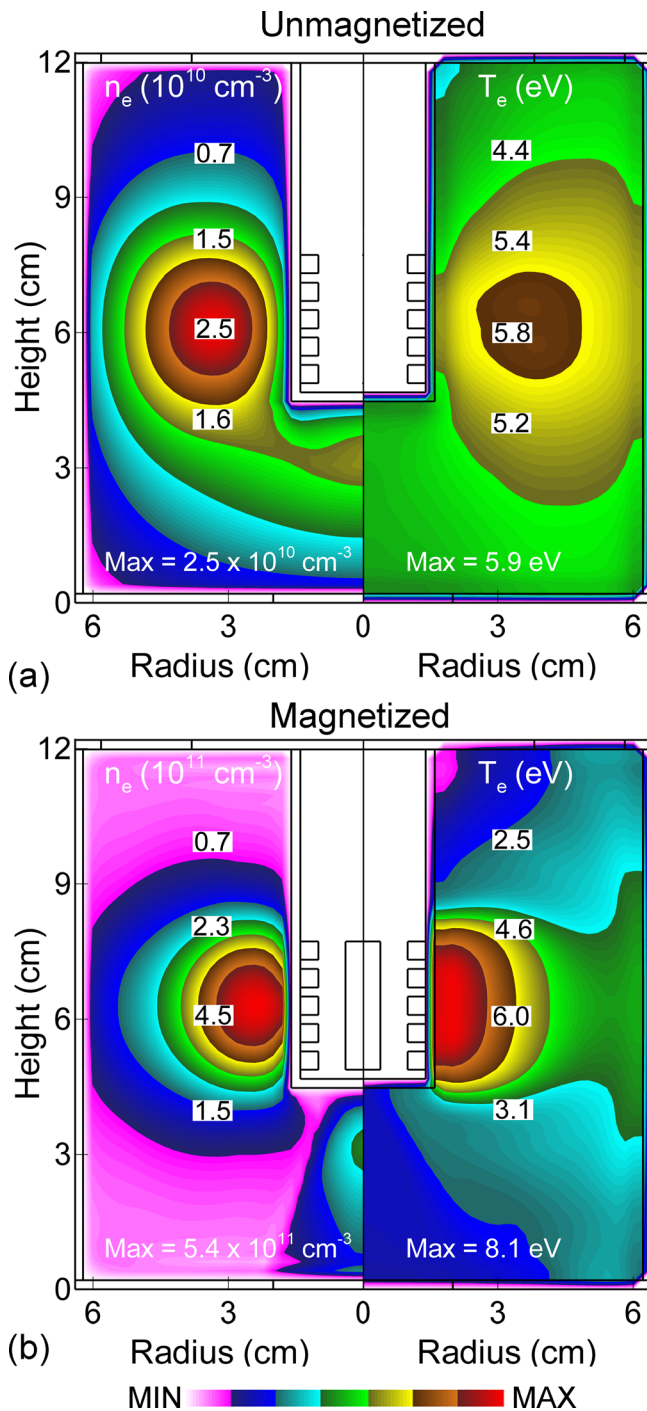


FIG. 3. Electron density and temperature for the base case conditions (3 mTorr, 100 W, and 5 MHz). (a) Unmagnetized and (b) magnetized conditions. With B_{ext} , the peak electron density and temperature increase and shift towards smaller radius.⁴

the maximum shifts to a smaller radius (from 3.3 cm to 2.3 cm). This shift is accompanied by an increase in the peak value of T_e from 5.9 to 8.1 eV, and a shift in the location of the peak of T_e from a radius of 3.8 cm to 2.1 cm. In the experiment,¹⁶ the peak electron density increases by nearly a factor of 30 (from $3 \times 10^{10} \text{ cm}^{-3}$ to $9 \times 10^{11} \text{ cm}^{-3}$) and the peak shifts from 3 cm to 2.3 cm. This is accompanied by an increase in the peak T_e from 6.3 eV to 17 eV, and a change in the spatial distribution of T_e from being uniform to peaking adjacent to the coil. (The absolute value of T_e near the

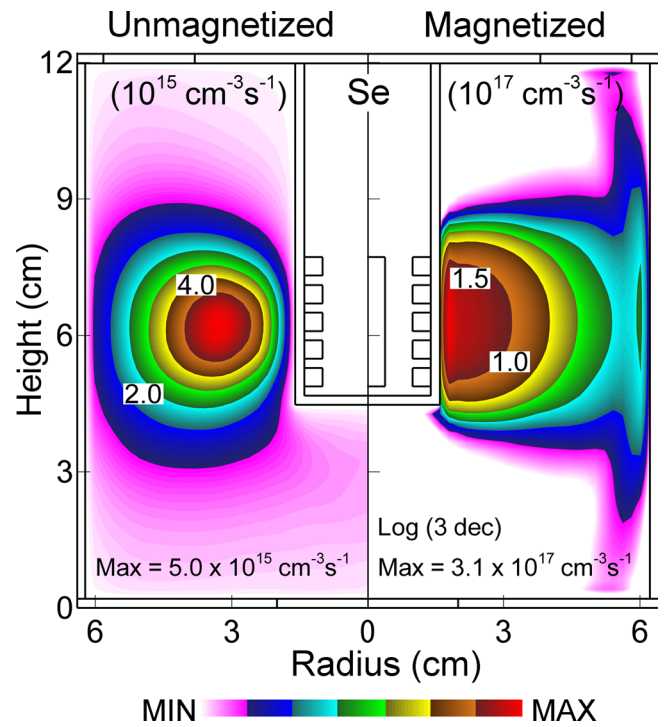


FIG. 4. Ionization rates for unmagnetized and magnetized discharges. Due to the enhanced tail of $f(\varepsilon)$ adjacent to the coils with B_{ext} , ionization rates locally increase by an order of magnitude.

dielectric window was likely overestimated in the experiment because of incomplete compensation of the RF plasma potential.¹⁶) With the magnetic field, the peak ionization rate increases by a factor of 60 (from $0.5 \times 10^{16} \text{ cm}^{-3} \text{ s}^{-1}$ to $3.0 \times 10^{17} \text{ cm}^{-3} \text{ s}^{-1}$) and shifts to a smaller radius (from 3.3 cm to 1.85 cm) due to the confinement of hot electrons at the smaller radius. The computed and experimental trends agree well.

The increases in peak electron density and ionization source with the magnetic field are not necessarily the best indication of ionization efficiency. The total power deposition is held constant and so, in some sense, the volume integrals of n_e and S_e may be better indications of efficiency than peak values. For example, the peak values of n_e and S_e both increase with the magnetic field however the peak values also occur at smaller radii in a smaller volume. So even though the peak value of n_e increases by a factor of 20, the volume integral of electron density increases by a factor of 11 (from 1.46×10^{13} to 1.67×10^{14}).

The electron energy probability functions (EEPFs), $f_p(\varepsilon)$, are different radial positions are compared with experimental results in Figs. 5 and 6. The n_e and T_e for these cases are in Fig. 7. For the unmagnetized case (Fig. 5), the computed $f_p(\varepsilon)$ is a weak function of radius and this is consistent with the experimental results, subject to some distortion in the experimental $f_p(\varepsilon)$ at low energy due to possible uncompensated rf plasma potential variation.¹⁶ The high conductivity of the plasma produced by electron-electron (e - e) collisions at low energy and the non-local character of the electron kinetics homogenizes $f_p(\varepsilon)$ over a large radius. The Maxwellian-like $f_p(\varepsilon)$ at energies less than the inelastic thresholds from the ground state, 11.5–16 eV, is due in part

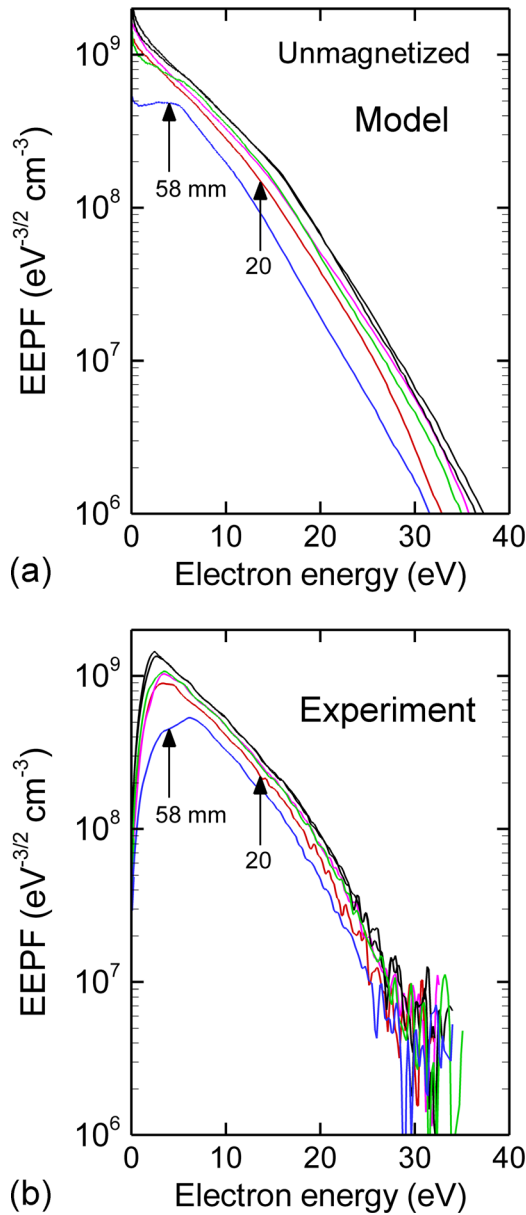


FIG. 5. Electron energy probability functions $f_P(\epsilon)$ at different radial positions without B_{ext} . (a) $f_P(\epsilon)$ predicted by the model and (b) measured in the experiment.¹⁶ $f_P(\epsilon)$ is not a sensitive function of radius. Experimental data were reprinted with permission from J. A. Monreal *et al.*, Phys. Plasmas **20**, 103504 (2013). Copyright (2013) American Institute of Physics.

to e - e collisions in the high conductivity plasma. There is a significant change in slope at the inelastic thresholds, which produces a Maxwellian appearing $f_P(\epsilon)$ tail. However, the tail of $f_P(\epsilon)$, particularly at large radius, is less influenced by e - e collisions since the frequency of these collisions scales as $\nu_{ee} \sim n_e \epsilon^{-3/2}$. The overall decrease in the value of $f_P(\epsilon)$ is due largely to the decrease in plasma density at large radius. Independent of probe distortion, there is an anomalous decrease in the low energy component of $f_P(\epsilon)$ at large radius, 58 mm, in both the experiment and model results. This apparent decrease at low energy is likely due to a decrease in the rate of e - e collisions, an augmentation of the tail of $f_P(\epsilon)$ due to long mean-free-path electrons and inefficient electron trapping of low energy electrons by the ambipolar electric field near the plasma boundary.

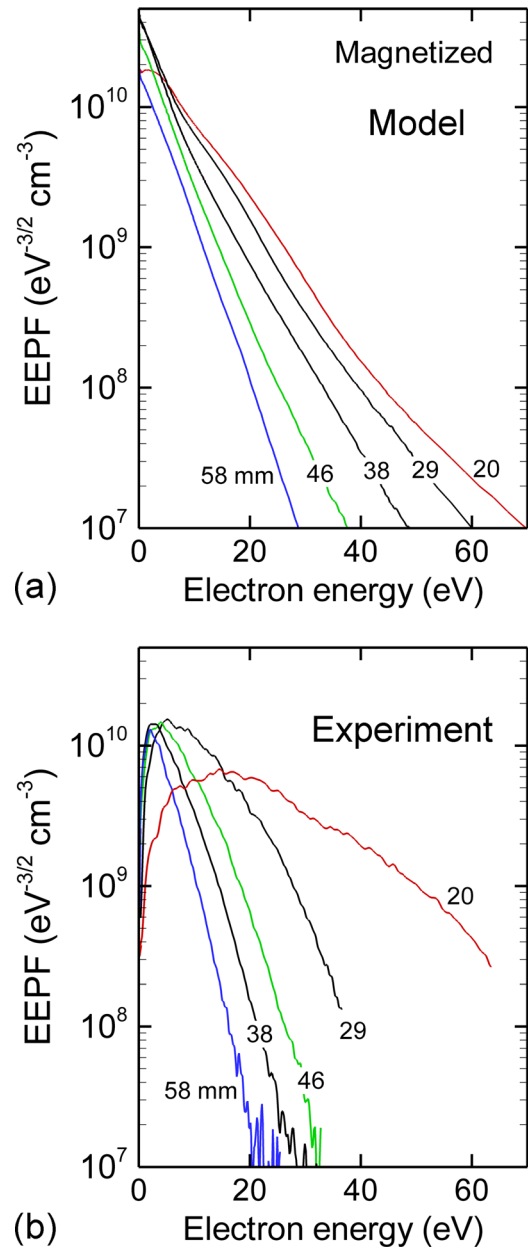


FIG. 6. Electron energy probability functions $f_P(\epsilon)$ at different radial positions with B_{ext} . (a) $f_P(\epsilon)$ predicted by the model and (b) measured in the experiment.¹⁶ The tail of $f_P(\epsilon)$ is raised at small radius due to the confinement of hot electrons, and reduced at large radius due to lack of long-mean-free path transport from the skin layer. Experimental data were reprinted with permission from J. A. Monreal *et al.*, Phys. Plasmas **20**, 103504 (2013). Copyright (2013) American Institute of Physics.

For the magnetized case (Fig. 6), $f_P(\epsilon)$ is a strong function of radius. Due to the reduction in the radial mobility and trapping of hot electrons produced adjacent to the coil where the electric and B_{ext} are largest, the population of high-energy electrons is significantly reduced at larger radii. The transition of electron kinetics from non-local to local by the magnetic field results in a closer correlation of the local rf-electric field with plasma properties. Since the electron density is higher and there are more e - e collisions, the distribution tends to be Maxwellian. The comparison to experiment is favorable though the curvature of the tail of the distribution at small radii is inverted.

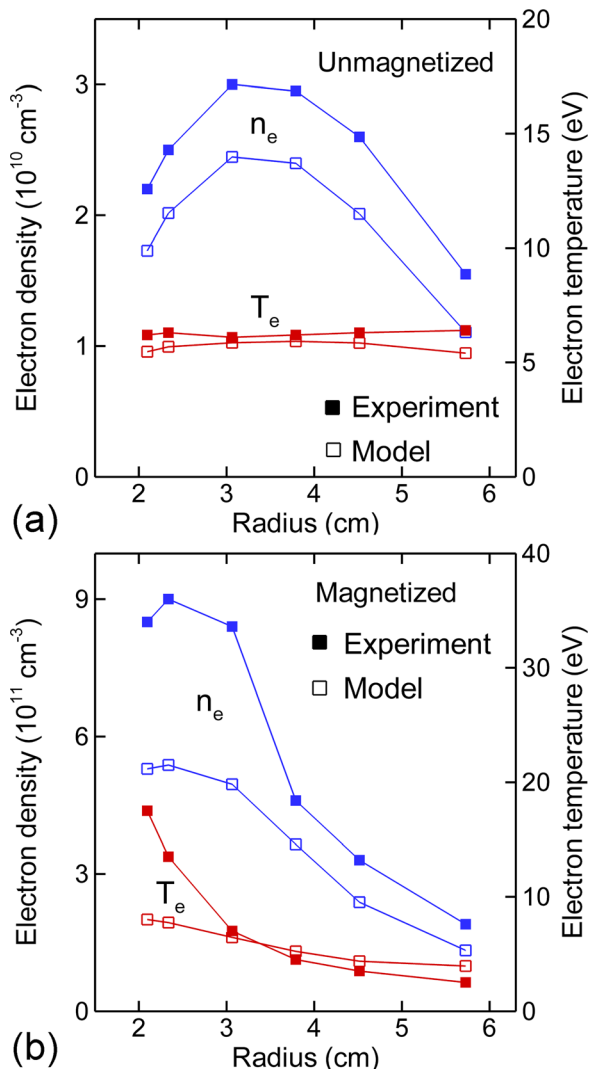


FIG. 7. Comparison of the electron density and temperature between the model and experiment¹⁶ (a) without B_{ext} and (b) with B_{ext} . By applying the external magnetic field, both the peak electron density increases and shifts towards smaller radius and the peak electron temperature shifts towards smaller radius. Experimental data were reprinted with permission from J. A. Monreal *et al.*, Phys. Plasmas **20**, 103504 (2013). Copyright (2013) American Institute of Physics.

Our working definition of energy relaxation distance, λ_e , is the characteristic distance traveled by an electron to lose its current energy.

$$\lambda_e^{-1}(\vec{r}) = \int_0^\infty f(\varepsilon, \vec{r}) \varepsilon^{1/2} \sum_{ij} \sigma_{ij}(\varepsilon) N_i(\vec{r}) \frac{\Delta \varepsilon_{ij}}{\varepsilon} d\varepsilon, \quad (12)$$

where σ_{ij} is the electron impact cross section for process j for collisions with species i having density N_i and with energy loss $\Delta \varepsilon_{ij}$. λ_e is then function of position because both $f(\varepsilon, \vec{r})$ and $N_i(\vec{r})$ may be functions of position. It is most common to define local transport as corresponding to conditions where $\lambda_e \ll L$ (where L is the characteristic size of the system) and non-local as corresponding to $\lambda_e \gg L$. In practice, λ_e does not necessarily correspond to the linear distance between the sites of energy loss collisions, but rather maps to the integral along the electron's path between these collisions. In magnetized systems, the integral along the

electron's helical trajectory between collisions on the magnetic field line can be much greater than the linear separation between those collisions. As a result, the conventional definition of local, $\lambda_e \ll L$, is not necessarily valid because λ_e could be much greater than L while the linear distance between collisions is much smaller than L .

In the absence of the magnetic field, the mean-free-path for energy loss at a radius of 2 cm is $\lambda_e = 740$ cm, which is much larger than the radius of the reactor. That is, $\lambda_e \gg L$. Although the majority of the electron heating occurs within the skin depth from the rf antenna, the momentum transfer relaxation length is $\lambda_m \approx 14$ cm, and so these hot electrons are distributed well beyond the skin depth. This non-local distribution is aided by the harmonic magnetic field that, on the average, produces a $\vec{v} \times \vec{B}$ pondermotive force that points radially outward from the skin depth. The $f_p(\varepsilon)$ are therefore fairly uniform across the radius, appearing close to Maxwellian due to the influence of e - e collisions at lower energies.

With the magnetic field, $\lambda_e = 490$ cm and $\lambda_m = 22$ cm. The increase in λ_m is largely due to a decrease in gas density by a factor of 1.7 due to more efficient gas heating with the magnetic field. λ_e decreases due to the change in $f_p(\varepsilon)$ in spite of the decrease in gas density which should otherwise lengthen λ_e as occurs for λ_m . Both with and without the magnetic field, $\lambda_e \gg L$. The local character of $f_p(\varepsilon)$ with the magnetic field is therefore not a consequence of the magnetic field producing $\lambda_e \ll L$. Rather the local character of $f_p(\varepsilon)$ is due to the electron's helical trajectory on the magnetic field line which enables a mean-free-path of distance to be traveled with a small change in radial position.

At a radius of 2.4 cm where the magnetic field is 100 G, the electron Larmor radius is ≈ 0.7 mm, the electron cyclotron frequency is $\omega_c \approx 1.8 \times 10^9 \text{ s}^{-1}$, the plasma frequency is $\omega_p \approx 4.1 \times 10^{10} \text{ s}^{-1}$ ($n_e = 5.4 \times 10^{11} \text{ cm}^{-3}$), and the electron-neutral collision frequency is $6 \times 10^6 \text{ s}^{-1}$. These conditions produce well magnetized electrons. The ambipolar diffusion coefficient parallel to the magnetic field is $3.2 \times 10^6 \text{ cm}^2 \text{ s}^{-1}$, while the diffusion coefficient perpendicular to the magnetic field is only $2.6 \times 10^4 \text{ cm}^2 \text{ s}^{-1}$. Electrons therefore have their energy loss collisions in close proximity to where they are accelerated, and so are confined to the skin depth. The tail of $f_p(\varepsilon)$ is therefore highest in the skin depth closest to the coil and monotonically decreases with increasing radius.

The differences in magnetization of low energy electrons compared to high energy electrons in static magnetic fields are not immediately clear. Colder electrons are probably in general more magnetized than hotter ones since their Larmor radius, r_L , is smaller, but this really only applies to conditions where the collision frequencies are equal. If the collision frequency of lower energy electrons is much greater than that for higher energy electrons, then the lower energy electrons will be less magnetized in spite of their smaller r_L . In any case, the model should capture these effects in the $f_p(\varepsilon)$ because the equations of motion of the electrons are being integrated with collisions occurring with energy resolved frequencies. That is, there are no assumptions being made about the relative values of r_L and D_\perp between low and high energy electrons.

n_e and T_e as a function of radius are compared with experimental values in Fig. 7 at the mid-height of the coil. In general, without B_{ext} , the electron density peaks near the center of the chamber with a small shift towards the coils due to isotropic ambipolar diffusion dominating charged particle loss. The computed and experimental electron densities agree to within 20%. T_e does not significantly vary with radius due to non-local kinetics dominating, and agreement with experiment is within about 10%. For the magnetized case, agreement is within 20% at large radius and 40%–50% at small radius. This difference is largely a consequence of there being more depletion of low energy electrons at high magnetic field (small radius) in the experiment than predicted by the model, some of which may be due to the lower efficiency of collecting low energy electrons with the probe and the previously mentioned insufficient rf compensation.¹⁶ The insufficient compensation for the rf plasma potential induced by polarization rf fields in the axial and radial directions led to distortion of $f_p(\varepsilon)$ measured at small radius. This distortion resulted in exaggerated values of the T_e and n_e inferred from the measured $f_p(\varepsilon)$. In the computed results, we have a small depletion of low energy electrons only at the smallest radius. There may also be a component of capacitive coupling or a Trivelpiece-Gould mode heating at small radius that is not accounted for in the model.

IV. SCALING WITH PRESSURE AND POWER

In this section, we discuss the electron energy distribution, $f(\varepsilon)$, as a function of pressure and power. We use $f(\varepsilon)$ here, instead of $f_p(\varepsilon)$, to emphasize the change in the fundamental distribution of electron energies independent of the change in electron density.

$f(\varepsilon)$ for unmagnetized and magnetized plasmas at the reference position (radius = 3 cm at height of the mid-coil as noted in Fig. 1(a) where $B = 57$ Gauss) are shown in Fig. 8 for pressures of 3–100 mTorr. T_e , n_e , and S_e are shown in Figs. 9–11. Since the shape of the plasma changes as pressure increases, $f(\varepsilon)$ at a fixed radius may reflect a combination of the change in pressure and change in shape. However, as shown in Fig. 9, although the peak T_e shifts to a smaller radius as pressure increases, the variation of T_e at a radius of 3 cm is mainly determined by the pressure. (Nevertheless, it is worth noting that if the $f(\varepsilon)$ had been compared at larger radius, differences could reflect both the shape and the pressure dependence.) Without B_{ext} , as the pressure increases, the tail of $f(\varepsilon)$ progressively becomes more cut-off at the threshold energy for excitation of the Ar(4s) manifold, approximately 12 eV. With B_{ext} , the tail of $f(\varepsilon)$ is more enhanced due to the confinement of the hot electrons and the reduction in diffusion cooling that naturally depletes the tail. As the pressure increases, the confinement effect diminishes due to the increase in collision frequency. At 100 mTorr, the electron-neutral collision frequency, $1.9 \times 10^8 \text{ s}^{-1}$, is approaching the cyclotron frequency ($\omega_c/2\pi = 1.6 \times 10^8 \text{ s}^{-1}$) at the reference position.

Without B_{ext} , T_e decreases while n_e increases as pressure increases due to a lower rate of loss by diffusion. The electron energy relaxation length (λ_e) decreases to 26 cm at

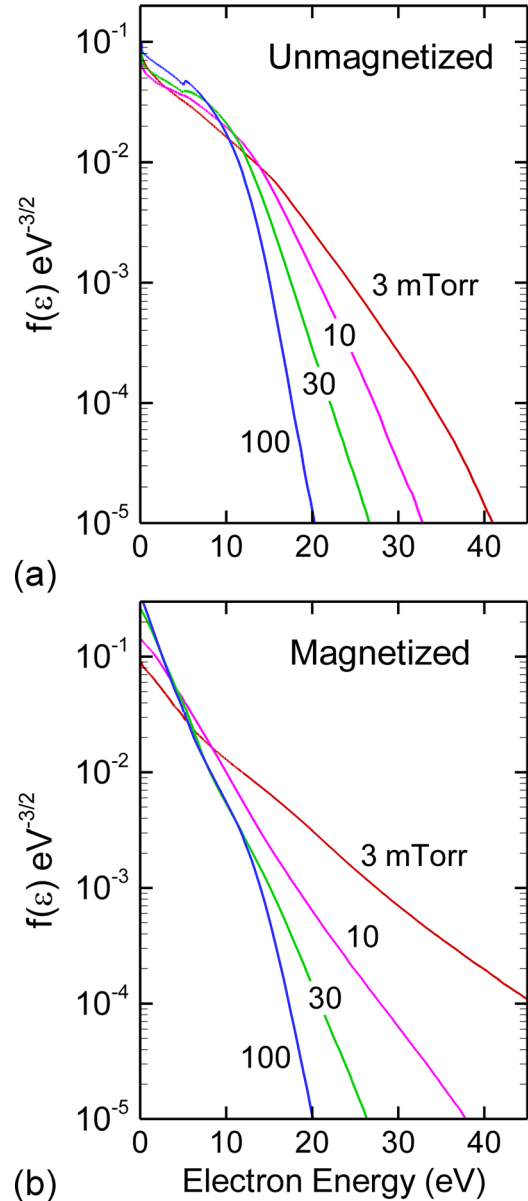


FIG. 8. Electron energy distributions functions for different pressures (a) without B_{ext} and (b) with B_{ext} . Without the magnetic field, the tail of the distribution is cutoff at the threshold energy for inelastic processes. With the magnetic field, the tail is enhanced at the lower pressure due to the reduction of diffusion cooling.

100 mTorr, which is beginning to approach the chamber radius. Therefore, T_e is fairly uniform across the chamber at 3 mTorr while there is significant radial variation at 100 mTorr. The radial dependence of n_e does not significantly change as the pressure increases over this range, with a small shift of the peak density towards smaller radius as the pressure increases. (The maximum in n_e is at a radius of 3.3 cm at 3 mTorr and 2.8 cm at 100 mTorr.) These trends indicate that the electron ionization source peaks at approximately the same position over this range of pressure, as shown in Fig. 11. The ionization rate $S_e = n_e(\vec{r})N_g \int_0^\infty f(\varepsilon, \vec{r}) \left(\frac{2\varepsilon}{m_e}\right)^{\frac{1}{2}} \sigma_{ion}(\varepsilon) d\varepsilon$ is determined by $f(\varepsilon, \vec{r})$, electron density (n_e), and neutral density (N_g). In the unmagnetized plasma, the

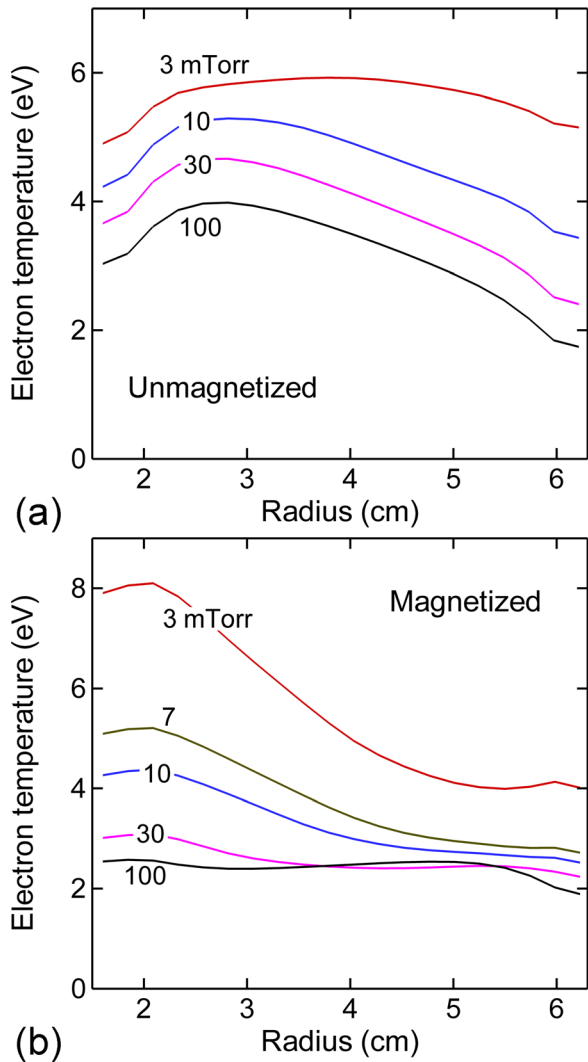


FIG. 9. Electron temperature as a function of radius for various pressures (a) without B_{ext} and (b) with B_{ext} . Without B_{ext} , T_e is fairly uniform at 3 mTorr. At higher pressures, T_e has a gradient due to the shorter mean free path. Without B_{ext} , the temperature becomes more uniform as pressure increases due to the increased collision frequency being commensurate with cyclotron frequency.

increase in n_e and N_g with increasing pressure is greater than the lowering of the tail of $f(\varepsilon)$. Therefore, the ionization rate increases as pressure increases. For the total power deposition to remain constant at 100 W, the volume integral $P = \int n_e(\vec{r})K_\varepsilon(\vec{r})N_g d^3r$ should remain constant, where K_ε is the rate coefficient for energy loss ($\text{eV}\cdot\text{cm}^3/\text{s}$). The lowering of the tail of $f(\varepsilon)$ decreases K_ε with increasing pressure faster than the increase in N_g , as shown in Fig. 12. Therefore, n_e must increase to deposit the same total power.

With B_{ext} , the peak plasma density is constant within less than a factor of two from 3–100 mTorr, which significantly differs from the unmagnetized case where the peak electron density increases with pressure. This behavior is partly explained by the shape of the plasma and dependence of K_ε with pressure. First, K_ε significantly decreases with increasing pressure which reflects the cut-off of the tail of $f(\varepsilon)$. In the low pressure regime, 3–30 mTorr, as pressure increases, electron kinetics transitions

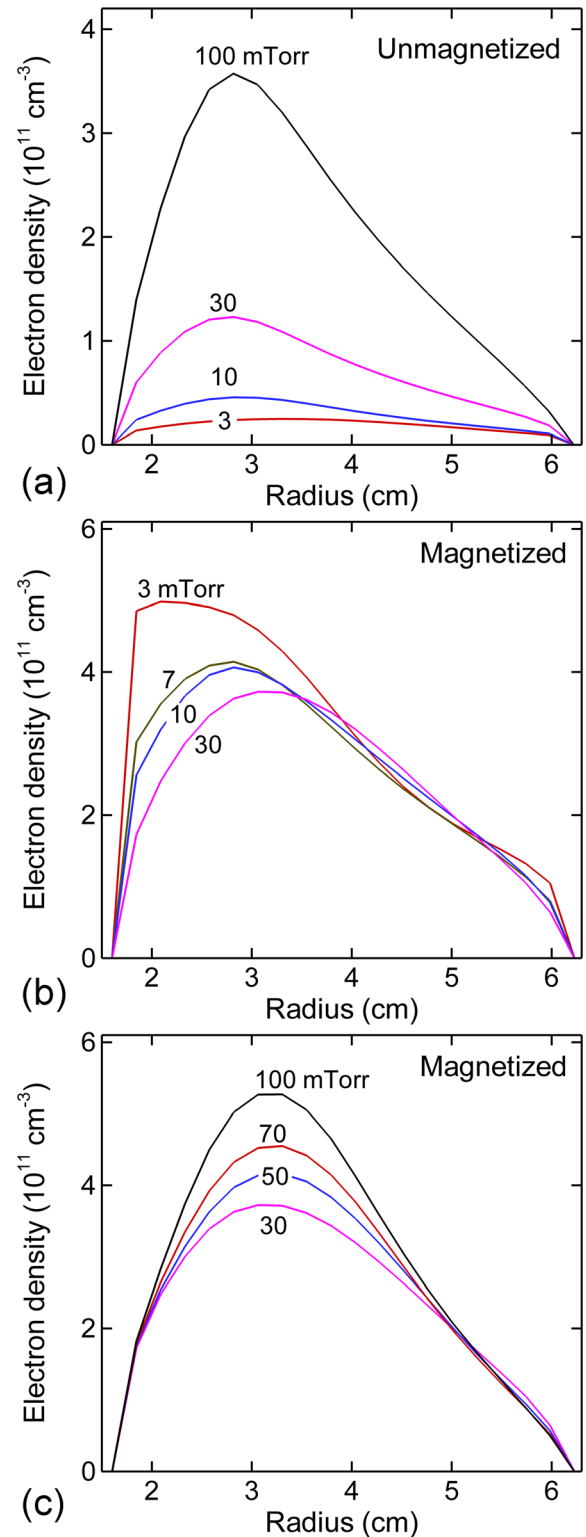


FIG. 10. Electron density as a function of radius (a) without B_{ext} for a pressure range of 3–100 mTorr, (b) with B_{ext} for 3–30 mTorr, and (c) with B_{ext} for 30–100 mTorr. Without B_{ext} , the peak electron density increases with pressure due to the reduced diffusion loss. With B_{ext} for 3–30 mTorr, the peak density decreases accompanied by a shift towards larger radius as pressure increases. Above 30 mTorr, the peak density increases with pressure.

from local to non-local and the peak electron density shifts to a larger radius (from 2.1 cm to 3.1 cm). At this larger radius, the incremental volume is larger. Although the peak electron density decreases by about 20% with

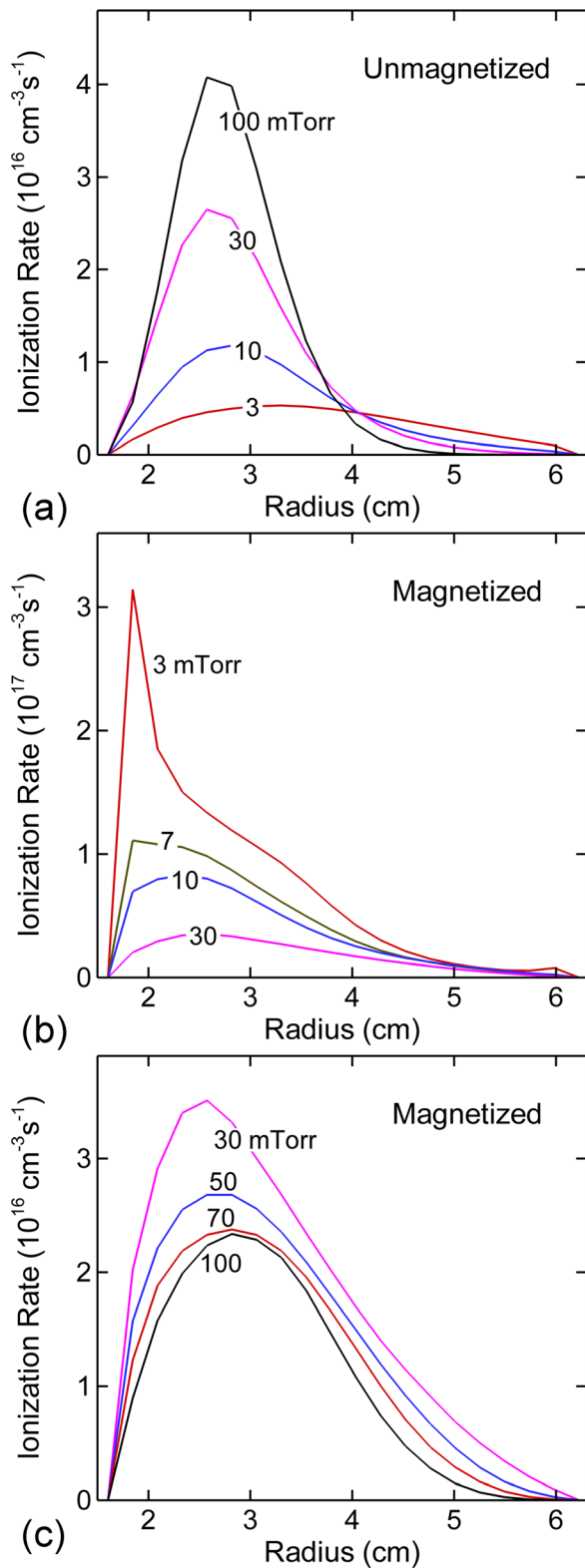


FIG. 11. Electron impact ionization rates as a function of radius (a) without B_{ext} for a pressure range of 3–100 mTorr, (b) with B_{ext} for 3–30 mTorr, and (c) with B_{ext} for 30–100 mTorr.

increasing pressure (from $5 \times 10^{11} \text{ cm}^{-3}$ at a radius of 2.1 cm to $3.7 \times 10^{11} \text{ cm}^{-3}$ at 3.1 cm), the volume integral of N_{gn_e} increases from 3 to 30 mTorr. This increase compensates for the decrease in K_e to keep power deposition constant.

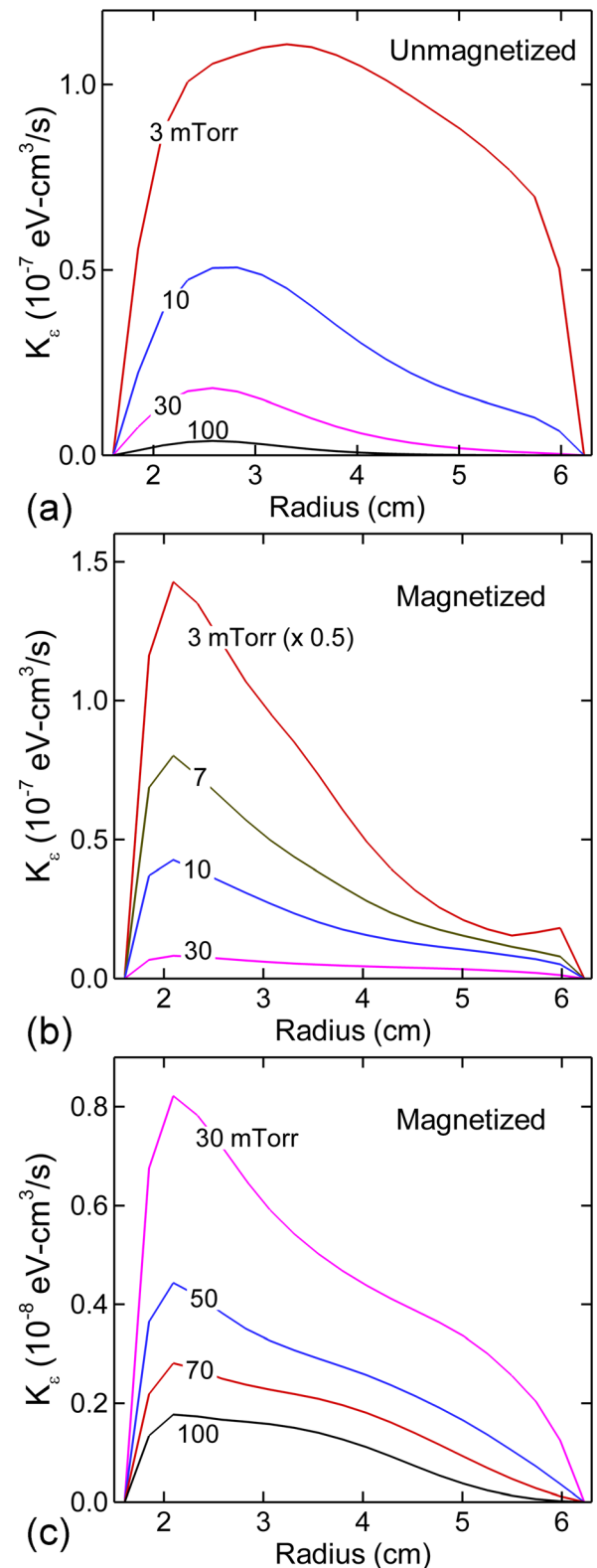


FIG. 12. Rate coefficient for electron energy loss as function of radius (a) without B_{ext} for a pressure range of 3–100 mTorr, (b) with B_{ext} for 3–30 mTorr, and (c) with B_{ext} for 30–100 mTorr.

In the high pressure regime (30–100 mTorr), as the pressure increases, the peak electron density stays at the same radius (same incremental volume) and so the peak value of n_e must increase in order to compensate for the decrease of K_e . At low pressure, the collision frequency is smaller than the

cyclotron frequency, which results in electron transport being local in spite of the low pressure. The plasma is skewed towards small radius where the ionization source, S_e , is maximum. At 100 mTorr, the plasma is magnetized at small radii (<3 cm) and unmagnetized at large radii (>4 cm), while based on pressure alone, electron transport is transitioning to being local at the higher pressure. The shape of the plasma therefore closely resembles that without B_{ext} .

Without B_{ext} , the $f(\varepsilon)$ are relatively insensitive to changes in power from 5–200 W, as shown in Fig. 13(a) for a pressure of 3 mTorr. The corresponding T_e and n_e as a function of radius are shown in Figs. 14 and 15. The $f(\varepsilon)$ have only minor differences in the tail as a function of power, producing T_e that are similarly a weak function of power. In quasi-steady state operation, $f(\varepsilon)$ is determined by

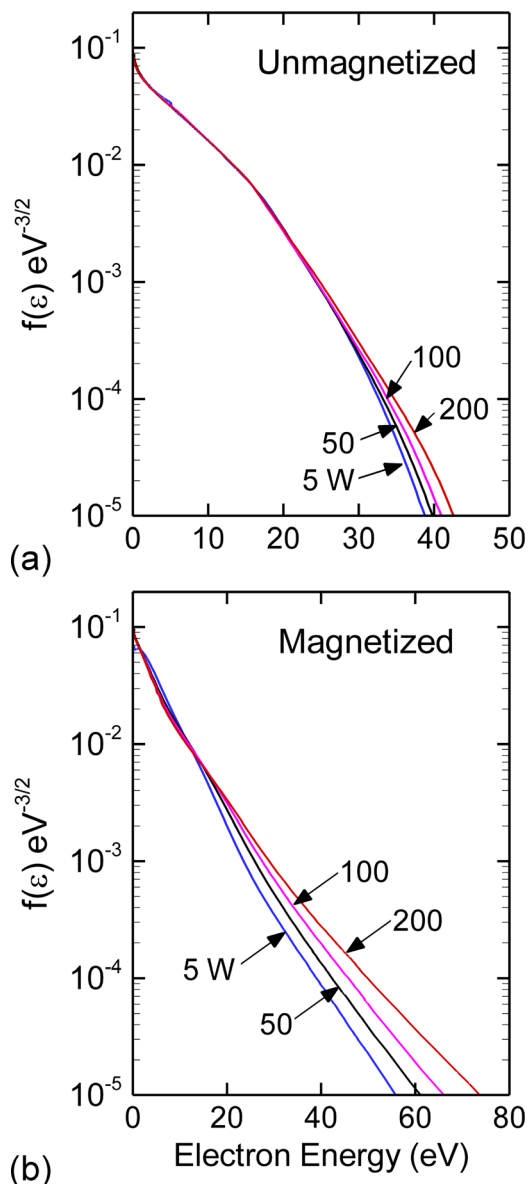


FIG. 13. Electron energy distributions for powers from 5–200 W (a) without B_{ext} and (b) with B_{ext} . The effect of power on $f(\varepsilon)$ is relatively small though this dependence is more acute with the magnetic field due to increasing rarefaction of the gas.

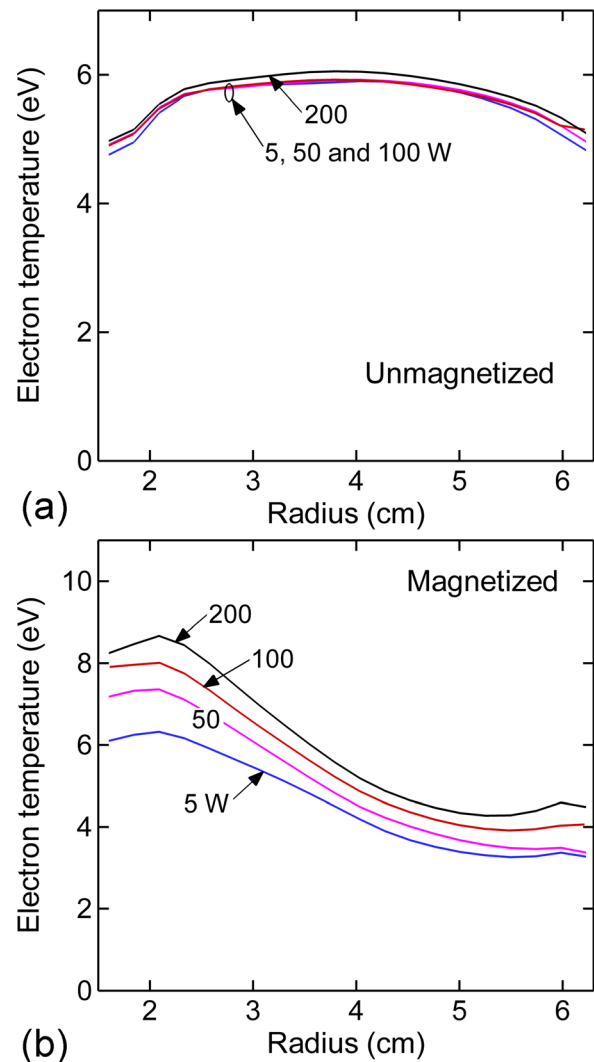


FIG. 14. Electron temperature for powers from 5–200 W (a) without B_{ext} and (b) with B_{ext} . The electron temperature does not vary with power without B_{ext} while temperature increases with power in the presence of the magnetic field.

a real-time balance between electron heating in the rf electric field, collisional energy losses and energetic electron losses to the walls. The resulting $f(\varepsilon)$ produces a real-time balance between electron sources and losses. Since electron loss by diffusion dominates for all powers, the electron loss rate by diffusion per electron is balanced by the rate of ionization per electron. The end result is that $f(\varepsilon)$ remains largely the same. Since $f(\varepsilon)$ and T_e are weak functions of power, K_e is also a weak function of power. n_e must then increase to enable $P = \int n_e(\vec{r})K_e(\vec{r})N_g d^3r$ to increase. The small lifting of the tail of the $f(\varepsilon)$ at higher power is likely due to a higher rate of long mean free path transport of high energy electrons from the skin depth.

With B_{ext} , $f(\varepsilon)$ is somewhat sensitive to power, as shown in Fig. 13. The tail of $f(\varepsilon)$ is raised with increasing power, which increases T_e (Fig. 14) and changes the radial dependence of n_e (Fig. 15), shifting the maximum in n_e to smaller radius. In the magnetized case, electrons exchange energy with other electrons through e - e collisions on the same magnetic field line, and that power stays on the magnetic line in

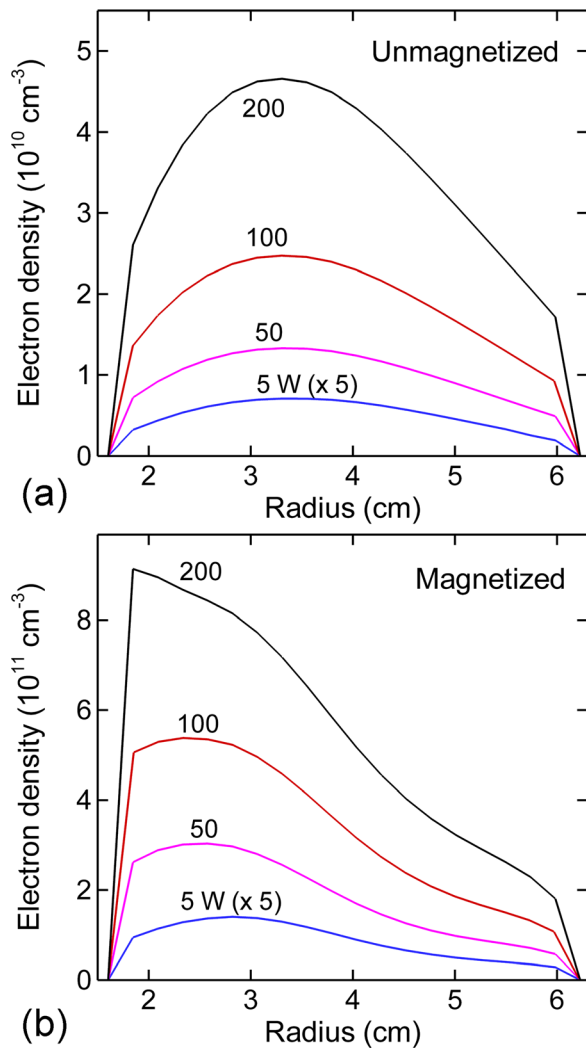


FIG. 15. Electron density for powers from 5–200 W (a) without B_{ext} and (b) with B_{ext} . The peak electron densities increase with power for both unmagnetized and magnetized conditions, though the latter also produces a shift in the location of the maximum.

the form of higher temperature electrons that produce an increase in local ionization. In the absence of B_{ext} , the thermal conductivity that results from the e - e collisions is isotropic and so the increase in power is shared more broadly in the plasma. Increasing the power from 5 W to 200 W with B_{ext} raises the gas temperature from 353 K to 782 K. The resulting rarefaction (effectively a lower pressure) and decrease in collision frequency then produces even more magnetized electrons that are more locally heated.

As the power increases, the maximum value of the electron density increases in the magnetized plasmas; while the position of the maximum shifts to smaller radii, an effect not seen in the unmagnetized case. This effect is similar to what is observed with a decrease in gas pressure (see Fig. 10) and so can be partly attributed to the decrease in gas density resulting from gas heating.^{41,42}

V. CONCLUDING REMARKS

The properties of ICPs with and without an externally applied static magnetic field have been computationally

investigated using results from a 2D plasma hydrodynamic model having a 3D electron Monte Carlo simulation including electron-electron collisions. Results are compared with experimental measurements of plasma properties and EEPFs, $f_P(\epsilon)$.^{16,23} In the absence of the magnetic field and at pressures of less than tens of mTorr, electron kinetics and the structure of the $f_P(\epsilon)$ are non-local. $f_P(\epsilon)$ and T_e are weak functions of radius. With the magnetic field, hot electrons generated in the skin depth adjacent to the antenna are impeded from diffusing radially outward and electron kinetics transitions to being local. The tail of $f_P(\epsilon)$ is enhanced due to the trapping of electrons on the axial magnetic field, which are heated by the inductively coupled electric field in the skin depth but are not able to diffuse to larger radii. The tail of $f_P(\epsilon)$ is depressed at locations outside the skin depth due to lack of long-mean-free transport of electrons from the skin depth to larger radii. The computed trends agree well with experiments. In the absence of the magnetic field, a transition from non-local-to local kinetics occurs with increasing pressure. With the magnetic field, electron kinetics first transitions to being less-local as the collision frequency increases and competes with cyclotron motion (20–30 mTorr), before becoming local due to the reduction in mean free path at even higher pressure (70–100 mTorr). However, even at 100 mTorr, where $f(\epsilon)$ and the spatial distribution of electron density are quite similar with and without the magnetic field, the magnetized case still has a 50% larger plasma density.

ACKNOWLEDGMENTS

The authors thank Dr. Valery Godyak for his extremely useful insights to and interpretation of the results discussed here. This work was supported by the Semiconductor Research Corp., Department of Energy Office of Fusion Energy Science (DE-SC0001319) and the National Science Foundation (CHE-1124724).

- ¹J. Asmussen, "Electron cyclotron resonance microwave discharges for etching and thin-film deposition," *J. Vac. Sci. Technol. A* **7**, 883 (1989).
- ²O. J. Glembocki, J. A. Tuchman, K. K. Ko, S. W. Pang, A. Giordana, R. Kaplan, and C. E. Stutz, "Effects of electron cyclotron resonance etching on the ambient (100) GaAs surface," *Appl. Phys. Lett.* **66**, 3054 (1995).
- ³R. A. Lindley, C. H. Bjorkman, H. Shan, K.-H. Ke, K. Doan, R. R. Mett, and M. Welch, "Magnetic field optimization in a dielectric magnetically enhanced reactive ion etch reactor to produce an instantaneously uniform plasma," *J. Vac. Sci. Technol. A* **16**, 1600 (1998).
- ⁴A. Herrick, A. J. Perry, and R. W. Boswell, "Etching silicon by SF₆ in a continuous and pulsed power helicon reactor," *J. Vac. Sci. Technol. A* **21**, 955 (2003).
- ⁵L. Wu, E. Ko, A. Dulkan, K. J. Park, S. Fields, K. Leeser, L. Meng, and D. N. Ruzic, "Flux and energy analysis of species in hollow cathode magnetron ionized physical vapor deposition of copper," *Rev. Sci. Instrum.* **81**, 123502 (2010).
- ⁶K. G. Kostov and J. J. Barroso, "Numerical simulation of magnetic-field-enhanced plasma immersion ion implantation in cylindrical geometry," *IEEE Trans. Plasma Sci.* **34**, 1127 (2006).
- ⁷D. Benyoucef, M. Yousfi, and B. Belmadani, "Self-consistent particle modeling of radio frequency discharge in Ar/O₂ mixtures: Effects of crossed electric and magnetic fields and partial pressure," *J. Appl. Phys.* **109**, 083304 (2011).
- ⁸W. Cronrath, N. Mayumi, M. D. Bowden, K. Uchino, M. Yoshida, and K. Muraoka, "A study of ion velocity distribution functions in processing plasmas produced by electron cyclotron discharges," *J. Appl. Phys.* **82**, 1036 (1997).

- ⁹D. D. Blackwell and F. F. Chen, "Time-resolved measurements of the electron energy distribution function in a helicon plasma," *Plasma Sources Sci. Technol.* **10**, 226 (2001).
- ¹⁰Z. Wang, S. A. Cohen, D. N. Ruzic, and M. J. Goekner, "Nitrogen atom energy distributions in a hollow-cathode planar sputtering magnetron," *Phys. Rev. E* **61**, 1904 (2000).
- ¹¹R. Doron, R. Arad, K. Tsigutkin, D. Osin, A. Weingarten, A. Starobinets, V. A. Bernshtam, E. Stambulchik, Yu. V. Ralchenko, Y. Maron, A. Fruchtmann, A. Fisher, J. D. Huba, and M. Roth, "Plasma dynamics in pulsed strong magnetic fields," *Phys. Plasmas* **11**, 2411 (2004).
- ¹²J. Bretagne, W. G. Graham, and M. B. Hopkins, "A comparison of experimental and theoretical electron energy distribution functions in a multi-cusp ion source," *J. Phys. D: Appl. Phys.* **24**, 668 (1991).
- ¹³G.-H. Kim, N. Hershkowitz, D. A. Diebold, and M.-H. Cho, "Magnetic and collisional effects on presheaths," *Phys. Plasmas* **2**, 3222 (1995).
- ¹⁴C. W. Chung, S. S. Kim, and H. Y. Chang, "Experimental measurement of the electron energy distribution function in the radio frequency electron cyclotron resonance inductive discharge," *Phys. Rev. E* **69**, 016406 (2004).
- ¹⁵A. Aanesland, J. Bredin, P. Chabert, and V. Godyak, "Electron energy distribution function and plasma parameters across magnetic filters," *Appl. Phys. Lett.* **100**, 044102 (2012).
- ¹⁶J. A. Monreal, P. Chabert, and V. Godyak, "Reduced electron temperature in a magnetized inductively coupled plasma with internal coil," *Phys. Plasmas* **20**, 103504 (2013).
- ¹⁷S. S. Kim, C. S. Chang, N. S. Yoon, and K. W. Whang, "Inductively coupled plasma heating in a weakly magnetized plasma," *Phys. Plasmas* **6**, 2926 (1999).
- ¹⁸O. V. Polomarov, C. E. Theodosiou, I. D. Kaganovich, B. N. Ramamurthi, and D. J. Economou, "Effectiveness of electron-cyclotron and transmission resonance heating in inductively coupled plasmas," *Phys. Plasmas* **12**, 104505 (2005).
- ¹⁹A. Rehman and Y. K. Pu, "Effect of electron thermal motion on plasma heating in a magnetized inductively coupled plasma," *Phys. Plasmas* **14**, 063503 (2007).
- ²⁰A. Rehman and J. K. Lee, "Effective viscosity model for electron heating in warm magnetized inductively coupled plasma discharges," *Phys. Plasmas* **16**, 083504 (2009).
- ²¹D. H. Kim and C.-M. Ryu, "Particle simulation of a magnetically enhanced dual-frequency capacitively coupled plasma," *J. Phys. D: Appl. Phys.* **41**, 015207 (2008).
- ²²L. D. Tsendin, "Current trends in electron kinetics of gas discharges," *Plasma Sources Sci. Technol.* **12**, S51 (2003).
- ²³V. A. Godyak, "EEDF control in gas discharge plasmas," *Phys. Plasmas* **20**, 101611 (2013).
- ²⁴V. Godyak and V. Kolobov, "Negative power absorption in inductively coupled plasma," *Phys. Rev. Lett.* **79**, 4589 (1997).
- ²⁵I. D. Kaganovich, O. V. Polomarov, and C. E. Theodosiou, "Revisiting the anomalous RF field penetration into a warm plasma," *IEEE Trans. Plasma Sci.* **34**, 696 (2006).
- ²⁶A. Maresca, K. Orlov, and U. Kortshagen, "Experimental study of diffusive cooling of electrons in a pulsed inductively coupled plasma," *Phys. Rev. E* **65**, 056405 (2002).
- ²⁷V. Godyak and B. Alexandrovich, "Plasma parameter evolution in a periodically pulsed ICP," in *Proceedings of the XXVII International Conference in Phenomena in Ionized Gases*, edited by Toshio Goto (Eindhoven, The Netherlands, 2005), Vol. 1, p.221.
- ²⁸H. S. Jun and H. Y. Chang, "Development of 40 MHz inductively coupled plasma source and frequency effects on plasma parameters," *Appl. Phys. Lett.* **92**, 041501 (2008).
- ²⁹U. Fantz, P. Franzen, W. Kraus, M. Berger, S. Christ-Koch, M. Fröschle, R. Gutser, B. Heinemann, C. Martens, P. McNeely, R. Riedl, E. Speth, and D. Wunderlich, "Negative ion RF sources for ITER NBI: Status of the development and recent achievements," *Plasma Phys. Controlled Fusion* **49**, B563 (2007).
- ³⁰M. J. Kushner, "Hybrid modelling of low temperature plasmas for fundamental investigations and equipment design," *J. Phys. D: Appl. Phys.* **42**, 194013 (2009).
- ³¹S. H. Song and M. J. Kushner, "Control of electron energy distributions and plasma characteristics of dual frequency, pulsed capacitively coupled plasmas sustained in Ar and Ar/CF₄/O₂," *Plasma Sources Sci. Technol.* **21**, 055028 (2012).
- ³²R. Kinder and M. J. Kushner, "Wave propagation and power deposition in magnetically enhanced inductively coupled and helicon plasma sources," *J. Vac. Sci. Technol. A* **19**, 76 (2001).
- ³³F. F. Chen, *Introduction to Plasma Physics and Controlled Fusion* (Springer, New York, 2006), p. 173.
- ³⁴W. H. Press, B. P. Flannery, S. A. Teukolsky, and W. T. Vetterling, *Numerical Recipes: The Art of Scientific Computing* (Cambridge University Press, Cambridge, 1986).
- ³⁵F. F. Chen, "Plasma ionization by helicon waves," *Plasma Phys. Controlled Fusion* **33**, 339 (1991).
- ³⁶K. Rajaraman and M. J. Kushner, "A Monte Carlo simulation of radiation trapping in electrodeless gas discharge lamps," *J. Phys. D: Appl. Phys.* **37**, 1780 (2004).
- ³⁷K. J. McCann and M. R. Flannery, "Photoionization of metastable rare-gas atoms (He*, Ne*, Ar*, Kr*, Xe*)," *Appl. Phys. Lett.* **31**, 599 (1977).
- ³⁸N. A. Dyatko, Y. Z. Ionikh, I. V. Kochetov, D. L. Marinov, A. V. Meshchanov, A. P. Napartovich, F. B. Petrov, and S. A. Starostin, "Experimental and theoretical study of the transition between diffuse and contracted forms of the glow discharge in argon," *J. Phys. D: Appl. Phys.* **41**, 055204 (2008).
- ³⁹A. Bogaerts and R. Gijbels, "Role of Ar²⁺ and Ar₂⁺ ions in a direct current argon glow discharge: A numerical description," *J. Appl. Phys.* **86**, 4124 (1999).
- ⁴⁰H.-J. Lee, H.-S. Tae, Y. T. Kim, and K.-W. Whang, "Electric field in magnetized inductively coupled plasma," *IEEE Trans. Plasma Sci.* **27**, 52 (1999).
- ⁴¹A. Fruchtmann, G. Makrinich, P. Chabert, and J.-M. Rax, "Enhanced plasma transport due to neutral depletion," *Phys. Rev. Lett.* **95**, 115002 (2005).
- ⁴²A. Aanesland, L. Liard, G. Leray, J. Jolly, and P. Chabert, "Direct measurements of neutral density depletion by two-photon absorption laser-induced fluorescence spectroscopy (TALIF)," *Appl. Phys. Lett.* **91**, 121502 (2007).